RSC Advances

PAPER

View Article Online
View Journal | View Issue

Cite this: *RSC Adv.*, 2016, **6**, 36954

Three dimensional manganese oxide on carbon nanotube hydrogels for asymmetric supercapacitors†

Hanlin Cheng,[a] Hai M. Duong*[a] and Daniel Jewell[b]

Received 31st January 2016
Accepted 30th March 2016

DOI: 10.1039/c6ra02858f

www.rsc.org/advances

In this article, we report the development of manganese oxide (Mn_3O_4) on carbon nanotube (CNT) hydrogels as binder-free electrodes for asymmetric supercapacitors. The CNT hydrogels consisting of three dimensionally inter-connected nanotubes are prepared *via* a facile sol–gel method. Afterwards, flower-like Mn_3O_4 is incorporated into CNT hydrogels using a pulse electrochemical deposition. Satisfactory electrochemical performance with a high specific capacitance of 182 F g^{-1} (473 mF cm^{-2}) is achieved. When employing activated carbon as negative electrodes, the assembled asymmetric supercapacitor exhibits a high potential window of 2 V to reach a specific energy of 26.6 W h kg^{-1} and a specific power of 5.2 kW kg^{-1}. These results are much better compared with the results from pure Mn_3O_4. The remarkable performance of our composites can be ascribed to a highly conducting CNT micro-scaffold and pseudocapacitive Mn_3O_4.

1. Introduction

The current global economy heavily relies on the consumption of traditional fossil fuels such as coal and petroleum. However, these non-renewable sources are expected to be depleted by the end of this century.[1] Besides that, the combustion of fossil fuels exacerbates global warming by emitting large amounts of greenhouse gases.[2] To address these challenges, various renewable energy sources such as solar, wind and geothermal energy have been explored.[3] Their power output, however, naturally fluctuates under diverse environmental situations, which increases the difficulty of an effective energy harvest.[4] In the light of this, electrochemical energy storage (EES) units are essential for better energy balance and coordination. Among various storage devices such as batteries and fuel cells, supercapacitors have drawn great attentions due to their moderate power and energy density.[5]

Supercapacitors can be categorized into electrochemical double layer capacitor (EDLC) and pseudocapacitor based on two different working mechanisms.[6] The first one takes an advantage of an electrochemical double layer formed at the electrode/electrolyte interface to store energy, while the second one utilizes fast redox chemical reactions.[7] For its resemblance to capacitors, the second category is named as 'pseudocapacitors'.[8] Various types of activated carbon (AC) have been extensively investigated as electrode materials for EDLC due to their high surface area.[9–11] Regardless of possessing ultrahigh cycling stability, AC suffers from a low specific capacitance. On the other hand, metal oxides/hydroxides and conducting polymers are widely used as pseudocapacitive materials because of their large theoretical capacitances.[12–14] Nevertheless, the poor cycling life and compromised power performance greatly limit their future development.[15] Therefore, it is essential to develop versatile composites to combine the merits of EDLC and pseudocapacitive materials.

Carbon nanotubes (CNTs), being the one-dimensional carbon allotrope with fantastic intrinsic properties, are widely used as a conductivity strengthening phase in composite design. To date, $Ni(OH)_2$/CNT,[16,17] MnO_2/CNT,[18,19] Co_3O_4/CNT,[20,21] and $NiCo_2O_4$/CNT[22] composite materials have been thoroughly investigated as supercapacitor electrode materials. Synthesized from the traditional routines, these composites exist in form of powders in which additional polymer binders have to be used for electrode fabrication. It is believed that the insulating nature of these polymer binders greatly hinders material performance.[23] In order to overcome this problem, binder-free CNT composites with three-dimensional (3D) architectures have been proposed. Generally, nickel and copper metal foams are used as the macro-scaffolds to grow CNTs, followed by incorporating pseudocapacitive materials into their 3D structure.[24–27]

Tang *et al.*[28] grew CNT on the nickel foam *via* chemical vapor deposition (CVD) and then successively synthesized $Ni(OH)_2$ on the nanotubes using a chemical bath deposition. As a result, a core/shell structure with ultrahigh capacitance (3300 F g^{-1})

[a]*Department of Mechanical Engineering, National University of Singapore, 9 Engineering Drive 1, EA-07-05, 117575 Singapore. E-mail: mpedhm@nus.edu.sg*
[b]*Department of Materials Science and Metallurgy, University of Cambridge, UK*

† Electronic supplementary information (ESI) available: Including additional SEM images, XRD patterns, EDX results and areal capacitances. See DOI: 10.1039/c6ra02858f

has been achieved. Similar methods have been used by Wu *et al.* to prepare 3D nickel cobalt oxide $NiCo_2O_4$/CNT nanostructure.[29] However, these methods only form a thin CNT film on nickel scaffold, leading to a small mass loading. By proper coating of these empty macro-pores, electrochemical performance of the supercapacitors can be further improved. From this perspective, Bryning *et al.* applied a sol–gel method to grow 3D CNT gels without using any metal foams thereby reached high porosity and electrical conductivity.[30] Unfortunately, these CNT gels suffered from low mechanical rigidity. Previously, we developed the $Ni(OH)_2$/CNT gels in which CNTs were used as a micro-scaffold and the nickel foam was used as a macro-scaffold.[31] Compared with the $Ni(OH)_2$, Mn_3O_4 has a larger potential window, better cycling stability and higher natural abundance and, thus, can serve as an ideal candidate for supercapacitor applications.[7]

In this work, we successfully developed Mn_3O_4/CNT hydrogels using a pulse electrochemical deposition method. The composite has achieved a balanced gravimetric capacitance of 182 F g^{-1} based on the total mass of the composite and areal capacitance of 473 mF cm^{-2} based on the geometric area of electrode. When using commercial AC as negative electrode material, the asymmetric supercapacitor can reach a stable potential as large as 2 V. It is found that a high specific energy of 26.6 W h kg^{-1} and specific power of 5.2 kW kg^{-1} can be realized. To the best of our knowledge, it is the first application of the 3D CNT hydrogel with Mn_3O_4 for supercapacitors.

2. Experimental section

2.1 Materials

CNTs (single-walled) composed of one third metallic and two thirds of semiconducting nanotubes were obtained from Chengdu Organic Chemicals Co Ltd. Manganese acetate tetrahydrate ($Mn(CH_3COO)_2 \cdot 4H_2O$), sodium dodecylbenzene sulfonate (SDBS), activated carbon (AC) and sodium sulfate (Na_2SO_4) were purchased from Sigma-Aldrich. Absolute ethanol and hydrochloric acid (HCl 37%) were obtained from Merck Pte Ltd. Nickel foams with thickness of 1.2 mm were bought from MTI Co. CNTs were purified by immersing into diluted HCl solution before use. Other chemicals were directly used without further purification.

2.2 Synthesis

Firstly, homogeneous dispersion consisting of CNTs (3 mg mL^{-1}) and SDBS (15 mg mL^{-1}) was prepared using probe sonication (60 W) for 30 min followed by 30 min bath sonication. Afterwards, cleaned nickel foams with area of 1 × 1 cm^2 were immersed in the as-prepared CNT dispersion under sonication for 10 min. Next, the CNT-coated nickel foams underwent aging for two days to form inter-connected CNT hydrogels (nanotube micro-scaffolds). The prepared hydrogels were subsequently washed using copious deionized (DI) water for a week to remove remaining surfactants. To obtain the Mn_3O_4/CNT hybrid hydrogels, plating solution consisting of 100 mM Na_2SO_4 and 10 mM $Mn(CH_3COO)_2$ was prepared in advance. The CNT hydrogels were immersed in the plating solution for 2 h to exchange the water inside with plating solutions. Next, pulse electrochemical deposition was carried out under a current of 2 mA cm^{-2} with an ON/OFF ratio of 10 s/20 s. After 150 cycles of deposition, the Mn_3O_4/CNT hydrogels were washed with DI water and stored in water overnight. For characterizations, the Mn_3O_4/CNT hydrogels were dried using critical carbon dioxide to maintain their original structure. Typically, the mass loadings of the CNT were 0.3–0.5 mg cm^{-2} and those of composites were in range of 2.2–2.6 mg cm^{-2}. For comparison, pure Mn_3O_4 was also deposited directly on the nickel foam based on the same protocols in the absence of CNTs.

2.3 Characterizations

The crystal structure of the Mn_3O_4/CNTs aerogels was determined by the X-ray diffractometer (XRD Shimazu 6000) with Cu K_α radiation. Sample morphology was investigated using the field emission scanning microscopy (FESEM Hitachi S4300). Transmission electron microscopy (TEM) analysis together with selected area electron diffraction (SAED) was performed on the JEOL 2010 transmission electron microscope for further investigation of the sample microstructures.

2.4 Electrochemical measurements

For electrochemical tests with three-electrode configuration, as-prepared Mn_3O_4/CNT composites were directly used as the working electrodes. Platinum (1 × 1 cm^2 in area) and saturated calomel electrode (SCE) were selected as the counter and reference electrodes, respectively. For the assembly of asymmetric supercapacitor, AC was used as the negative electrodes and Mn_3O_4 or Mn_3O_4/CNT hydrogel was used as the positive electrodes. The mass ratio between AC and Mn_3O_4/CNT was 2 : 1 and the ratio between the AC and Mn_3O_4 was 3 : 2 based on charge balance.[32] The asymmetric cells were assembled in swagelok cells with porous cellulose membrane as separators. All electrochemical measurements were carried out in 0.5 M Na_2SO_4 electrolyte. Cyclic voltammetry (CV), galvanostatic charge/discharge (GCD) and electrochemical impedance spectroscopy (EIS) were conducted on the Solartron 1287 electrochemical workstation. Calculations of the specific capacitance, specific energy and specific power were based on followed equations:[33]

$$C_s = \frac{\int I\,dV}{2mv\Delta V} \quad (1)$$

$$C_s = \frac{I\Delta t}{m\Delta V} \quad (2)$$

$$E = \frac{1}{2} C_s \Delta V^2 \times \frac{1000}{3600} \quad (3)$$

$$P = \frac{E}{\Delta t} \times 3600 \quad (4)$$

where C_s is the specific capacitance (F g^{-1}), I is the current (A), v is the scan rate (V s^{-1}) in CV tests, ΔV is the potential window

(V), Δt is the discharge time (s), E is the specific energy (W h kg^{-1}) and P is the specific power (W kg^{-1}). For asymmetric supercapacitor tests, m is the total mass (g) of AC and composites on both electrodes.

3. Results and discussions

3.1 Structures and morphologies

The hydrogel composites are synthesized according to the procedure illustrated in Fig. 1. The CNT dispersion undergoes the stage of gelation in ambient atmosphere for two days to form the inter-connected structure, which is reported in our previous work.[31] The formation of the CNT 3D network is caused by the strong van der Waals interactions between nanotubes. When placing the CNT hydrogel at the anode for deposition, manganese ions dissolved in water were oxidized under the positive voltage to give Mn_3O_4 precipitation at the CNT hydrogels described by following equation:[34]

$$4H_2O + 3Mn^{2+} = Mn_3O_4 + 2e^- + 8H^+ \quad (5)$$

Different from the galvanostatic or potentiostatic depositions, we apply a pulse deposition technique to tune Mn_3O_4 properties (Fig. S1†). During the "ON" period, the Mn_3O_4 are grown on the CNTs under a constant current. At the "OFF" stage, the current is set to zero to facilitate the ion diffusion from the central plating solution, considering the large thickness of the prepared hydrogels. As a result, morphology can be carefully controlled to avoid any unwanted agglomerations of active materials.

Fig. 2 presents morphology of the Mn_3O_4 and Mn_3O_4/CNT composites. Without the 3D inter-connected CNT networks, Mn_3O_4 merely stay at the surface of nickel foam, leaving majority of the macro-pores in the nickel foams unoccupied (Fig. 2a). With high magnification shown in Fig. 2b, we can see that the Mn_3O_4 is composed of severely stacked nanoparticles. This kind of agglomerations will not only hinder the ion diffusion but also extend the electron pathways, leading to poor electrochemical performance.[35] For the pristine CNT hydrogels deposited inside the nickel foam, they presented a network consisting of bundled nanotubes (Fig. S2†), which also can be found in our previous report.[31] While for the Mn_3O_4/CNT, the hydrogel fully occupies the macro-pores inside the nickel foams (Fig. 2c). In this architecture, CNT hydrogel serves as a micro-scaffold for electron transport and Mn_3O_4 plays a role of capacitance enhancer. The CNT micro-scaffold and Mn_3O_4 with

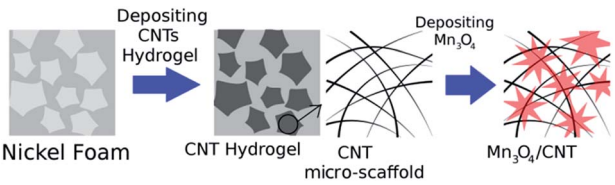

Fig. 1 Schematic illustration of preparation of the Mn_3O_4/CNT composite.

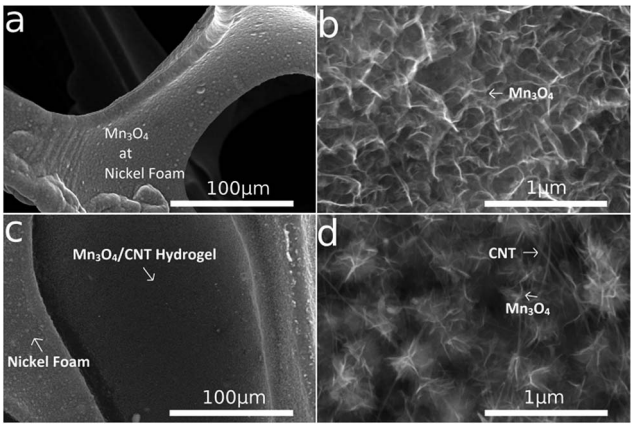

Fig. 2 FESEM images of Mn_3O_4 on the nickel foam at (a) low and (b) high magnification; the Mn_3O_4/CNT hydrogel at (c) low, and (d) high magnification.

higher magnification can be seen in the Fig. 2d. The CNT micro-scaffold presents the three-dimensional (3D) random inter-connected structure with homogeneously deposited Mn_3O_4 nano-flowers with a typical size of 300–400 nm. The flower-like Mn_3O_4 morphology can be ascribed to a controlled pulse deposition method in which Mn_3O_4 replicates the CNT patterns. The high transparency of Mn_3O_4 also indicates their ultrathin nature. The mesopores woven from CNTs are believed to effectively facilitate the ion diffusion process and boost the device performance. It is also worth noting that the CNT hydrogel not only fill the macropores inside the nickel foam but also cover the nickel foam backbones as thin layers (Fig. S3†). As a result, CNTs are inclined to grow on nanotubes both inside nickel foam and on nickel foam backbone surface.

More detailed micro-structure information of materials is investigated by TEM. For the nickel foam directly coated with Mn_3O_4 (Fig. 3a), manganese oxide phase consists of aggregated secondary particles with an average size around 50 nm. For the Mn_3O_4/CNT composite (Fig. 3b), we see that nanotubes form several bundles with a diameter around 10 nm, composing a micro-scaffold. The bundling of CNTs is probably caused by capillary force during the gelation period. This kind of micro-scaffold not only will improve the electrical conductivity of the electrode materials but also be effective in preventing Mn_3O_4 aggregation. Moreover, Mn_3O_4 is presented as the ultrathin flakes in the composite indicated by their curled peripheral edges. From the SAED images in Fig. 3c and d, the diffraction patterns can be ascribed to (103), (004), (224) crystal planes of Mn_3O_4 (JCPDS no. 18-0803). No diffraction pattern from CNTs is found due to their low content in the composite.

Typical XRD patterns of the pure Mn_3O_4 and Mn_3O_4/CNT hydrogel composite are presented in Fig. S4.† Three main peaks coming from the nickel foam can be easily identified. With a careful observation, peaks located at 34.7°, 39.1° can be ascribed to the tetragonal-phase Mn_3O_4.[36] Compared with peaks from the nickel foam, the Mn_3O_4 peaks have much smaller intensity, which might be attributable to two aspects. One possible reason is that the hydrogels have a low density, making

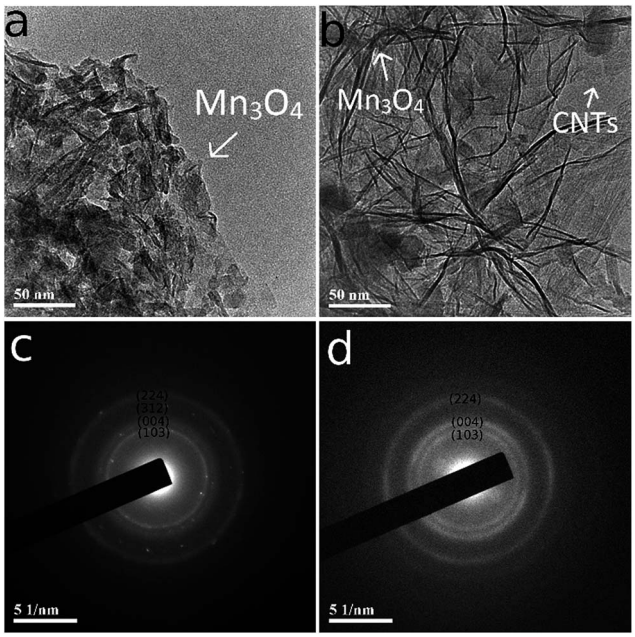

Fig. 3 TEM images of the (a) Mn_3O_4, (b) Mn_3O_4/CNT hydrogel; SAED patterns of (c) Mn_3O_4, and (d) Mn_3O_4/CNT composites.

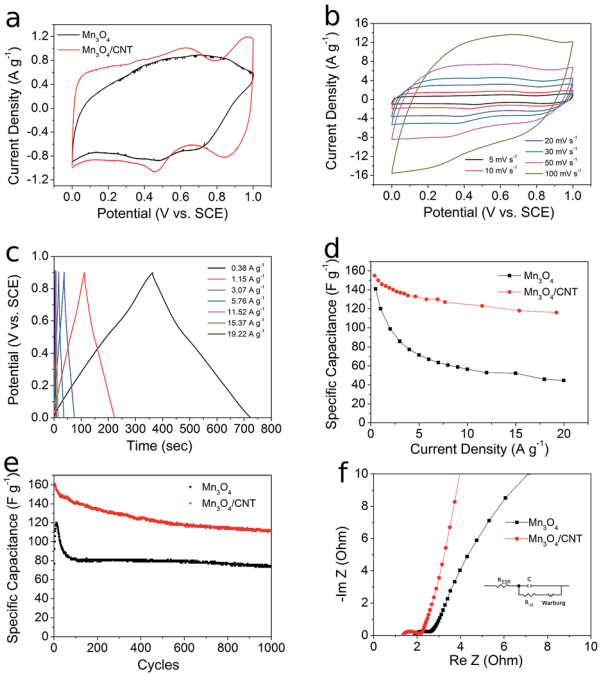

Fig. 4 Electrochemical performance of Mn_3O_4 and Mn_3O_4/CNT: (a) CV curves at low scan rate of 5 mV s^{-1}, (b) CV of the Mn_3O_4/CNT hydrogel at different scan rates, (c) GCD curve of Mn_3O_4/CNT at different current densities, (d) specific capacitance calculated from tests, (e) long term cycling performance, and (f) EIS results.

them highly transparent to the X-rays. The other possible reason is the poor crystallinity of Mn_3O_4, which is synthesized at room temperature.[37] The composition of the samples are also confirmed by the energy-dispersive X-ray spectroscopy (EDX) in which the atomic ratios between manganese and oxygen are closed to 3 : 4 (Fig. S5 and S6†).

3.2 Electrochemical performances

Fig. 4 presents the electrochemical performance of the Mn_3O_4 and Mn_3O_4/CNT composites tested with three-electrode configuration. Fig. 4a displays the CV curves of the Mn_3O_4 and Mn_3O_4/CNT at 5 mV s^{-1}. Compared with the Mn_3O_4, our developed 3D hydrogel composite exhibits a larger enclosed area, suggesting a higher specific capacitance. A pair of anodic/cathodic peaks of Mn_3O_4/CNT is found at 0.62 and 0.47 V, respectively, due to the redox nature of Mn_3O_4.[38] We interestingly find this pair of peak does not appear in the pure Mn_3O_4 because of a large resistance in the absence of the conductive CNTs. CV curves at different scan rates from 5 to 100 mV s^{-1} of the Mn_3O_4/CNT are given in Fig. 4b. A mirror-image feature demonstrates a good reversibility of the electrode materials. Contributed to high electrical conductivity of the 3D CNT structure, the CV loop still maintains almost a rectangular shape at a high scan rate of 100 mV s^{-1}. The calculated specific capacitances are 182 at 2 mV s^{-1} and 91 F g^{-1} at 100 mV s^{-1}, respectively. It is worth noting that the specific capacitances of manganese oxides are strongly related to the thickness of the materials.[39] Depositing thin layer material can dramatically improve the gravimetric capacitance. Unfortunately, this strategy usually results in an ultralow areal and volumetric capacitance, limiting the application of materials. For example, specific capacitances of more than 200 F g^{-1} have been reported for Mn_3O_4 previously, they either calculated capacitance merely based on Mn_3O_4 or applied a strategy on a basis of ultralow mass loading (<1 mg cm^{-2}) of active materials,[40–43] suffering a low areal capacitance. Nevertheless, for our composite, due to a large mass loading over ~2 mg cm^{-2}, high areal capacitance of 400 mF cm^{-2} can be reached (Fig. S7†). For our composites, the main roles of the CNTs in this composite are to enhance the conductivity and prevent Mn_3O_4 agglomeration, instead of the capacitance provider. GCD curves above of Mn_3O_4/CNT with different specific currents from 0.38 to 19.22 A g^{-1} are given in the Fig. 4c. The near-linear charge and discharge curves with negligible curvature reflect ideal capacitor behaviour. As seen in Fig. 4d, in contrast to pure Mn_3O_4 materials, the Mn_3O_4/CNT composite not only presents a higher capacitance at low discharge rate but also a good retention (71.6%) at high discharge rate.

The cycling performance of the Mn_3O_4 and Mn_3O_4/CNT are shown in Fig. 4e. Mn_3O_4/CNT presents a gradual capacitance drop to 1000th cycles with a final retention of 68.9%. For Mn_3O_4, a sharp capacitance drop is found after the initial activation capacitance. Then the specific capacitance keeps stable at about 80 F g^{-1}. The final specific capacitance is only 61.7% of the stable capacitance. Fig. 4f shows the EIS results of the Mn_3O_4 and Mn_3O_4/CNT composite. Based on the embedded equivalent circuit, the equivalent series resistances (ESR) of Mn_3O_4 and Mn_3O_4/CNT are 1.95 and 1.41 ohm, which represent the internal resistance of electrode, electrolyte and connecting

wires.[44] The smaller ESR of the Mn_3O_4 is attributable to the good host/guest materials interface between CNTs and Mn_3O_4, which effectively facilitates the electron transport process.

Considering a scalable production, AC is chosen as the negative electrode material to assembly an asymmetric supercapacitor. The CV curves at 30 mV s^{-1} of negative (AC) and positive (Mn_3O_4/CNT) electrode are presented in Fig. 5a. The AC processes a working potential ranging from −1 to 0 V and at the same time the Mn_3O_4/CNT hydrogel can successfully work within a potential range of 0–1 V. Therefore, the potential window of the asymmetric supercapacitor should be around 2 V. In order to demonstrate this estimation, CV tests of Mn_3O_4/CNT based asymmetric supercapacitor are carried out as given in the Fig. 5b. Rectangular loops can be observed with a potential window extending from 1 to 2 V, suggesting a good stability under higher potential. The larger working potential range also increased specific capacitance, indicated by a current increasing. The improved electrochemical performance under higher potential is related to the deeper activated Mn_3O_4. The GCD profiles of asymmetric supercapacitors using Mn_3O_4/CNT composites are displayed in Fig. 5c. A potential as high as 2 V can be guaranteed at the discharge rate from 0.5 to 10 A g^{-1}. Higher specific capacitance of Mn_3O_4/CNT compared with Mn_3O_4 benefits from the better electrochemical performance of positive electrode (Fig. 5d).

The cycling stability of two kinds of the asymmetric supercapacitors is shown in Fig. 6a. Initial activations are found for both Mn_3O_4 and Mn_3O_4/CNT which are associated with the electrolyte infiltration. After the short activation process, the Mn_3O_4/CNT composite could reach a stable specific capacitance above 25 F g^{-1} and achieved a good retention of 103.9% after 1000^{th} cycling. While for Mn_3O_4, only 84.0% of original capacitance is reserved. It is interesting to find there is a discrepancy of cycling stability tested with two-electrode and three-electrode configuration. We propose there two reasons to explain. Firstly,

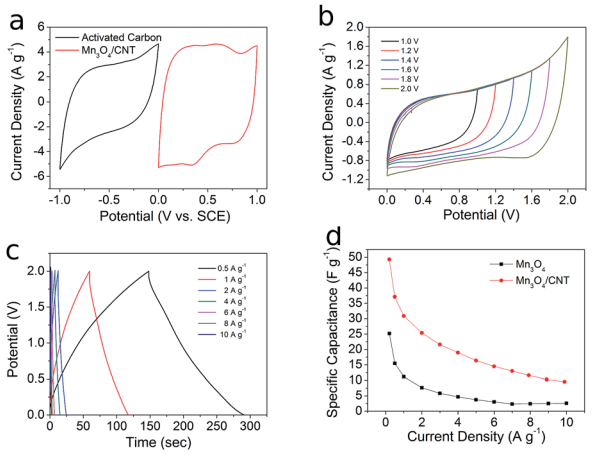

Fig. 5 Electrochemical performance of the asymmetric supercapacitor: (a) comparative CV of AC (black) and the Mn_3O_4/CNT hydrogel (red) at 30 mV s^{-1}, (b) CV of the asymmetric supercapacitor measured at different potentials at 30 mV s^{-1}, (c) GCD curves of the asymmetric supercapacitor at different current densities, and (d) specific capacitances from GCD tests.

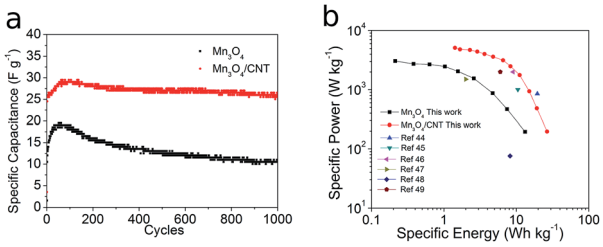

Fig. 6 (a) Cycling stability and (b) Ragone plot of asymmetric supercapacitors.

in three-electrode configuration, the composite was connected to the electrical wire using a simple conducting alligator and there is no other external force between the testing material and outer circuit. As a result, the any kind of fracture of materials due to cycling will directly drop into the electrolyte, causing the capacitance degradation. While in two-electrode configuration, the negative electrode, separator and positive electrodes were assembled in a swagelok cell. Under a tightening force from screw thread, even the fractured material is still in contact with the nickel foam, leading to a better cycling stability. Secondly, though the three-electrode cell was sealed using parafilm during the cycling performance, the sealing capability is not as good as ones with swagelok cell. Thus the degradation of the electrolyte might cause the cycling drop. To understand the power and energy performance of the assembled asymmetric supercapacitors, Ragone plot is given in Fig. 6b. High specific energy of 26.6 W h kg^{-1} and 5.6 kW kg^{-1} are achieved for Mn_3O_4/CNT, which is better than the pure Mn_3O_4 and other related reports.[44–49]

To further reveal the degradation mechanism of the electrode materials, we have characterized our sample using FESEM after cycling tests (Fig. 7). As can be seen in Fig. 7a, a large number of the tiny surface agglomerations have been observed for Mn_3O_4. The large surface changes compared to the pristine Mn_3O_4 can be attributed to the structural changes from surficial ion intercalation in the long term cycling test. For the Mn_3O_4/CNT composite (Fig. 7b), we can also observe morphology changes with bundled CNTs. This kind of morphology evolution is responsible for the capacitance degradation after activation period (~100^{th} cycle). However, due to the electron pathways established by CNTs and the ultrathin nature of Mn_3O_4, the composite is still capable to maintain its majority of its original capacitance.

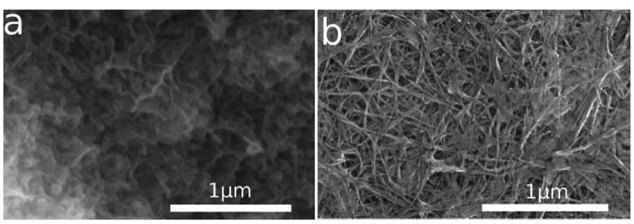

Fig. 7 FESEM images of (a) Mn_3O_4 and (b) the Mn_3O_4/CNT hydrogel after cycling.

4. Conclusions

In summary, we have successfully developed the Mn_3O_4/CNT hydrogels for supercapacitor applications. By utilizing a pulse electrochemical deposition, a high areal capacitance above 473 mF cm^{-2} can be achieved. The assembled asymmetric supercapacitor can reach a potential as high as 2 V in the aqueous electrolyte. Compared with the single-component Mn_3O_4 deposited on nickel foams, Mn_3O_4/CNT hydrogel has shown superior electrochemical performance both in higher capacitance and better cycling stability. This improvement can be attributed to the advantages of the CNT micro-scaffold, which (1) serving as electron transport highway and (2) inhibiting serious aggregation of active materials. We believe our prepared composites may also have applications in the field of battery electrodes and electrochemical catalysis.

Acknowledgements

We would like to take this opportunity to thanks Environmental Technology Program R-265-000-450-490 and Defence Research and Technology of MINDEF-R-394-001-077-232 for financial support. We are also grateful to Prof Lu Li from Department of Mechanical Engineering, NUS, for helpful discussion.

Notes and references

1 N. Armaroli and V. Balzani, *Energy Environ. Sci.*, 2011, **4**, 3193–3222.
2 A. Laurent and N. Espinosa, *Energy Environ. Sci.*, 2015, **8**, 689–701.
3 M. Z. Jacobson, *Energy Environ. Sci.*, 2009, **2**, 148–173.
4 Z. Yang, J. Zhang, M. C. W. Kintner-Meyer, X. Lu, D. Choi, J. P. Lemmon and J. Liu, *Chem. Rev.*, 2011, **111**, 3577–3613.
5 M. Winter and R. Brodd, *Chem. Rev.*, 2004, **104**, 4245–4269.
6 B. E. Conway, *Electrochemical Supercapacitors*, Kluwer Academic/Plenum Press, New York, 1999.
7 P. Simon and Y. Gogotsi, *Nat. Mater.*, 2008, **7**, 845–854.
8 L. L. Zhang and X. S. Zhao, *Chem. Soc. Rev.*, 2009, **38**, 2520–2531.
9 J. Chang, Z. Gao, X. Wang, D. Wu, F. Xu, X. Wang, Y. Guo and K. Jiang, *Electrochim. Acta*, 2015, **157**, 290–298.
10 F. Gao, G. Shao, J. Qu, S. Lv, Y. Li and M. Wu, *Electrochim. Acta*, 2015, **155**, 201–208.
11 D. Liu, W. Zhang, H. Lin, Y. Li, H. Lu and Y. Wang, *RSC Adv.*, 2015, **5**, 19294–19300.
12 J. Yan, Q. Wang, T. Wei and Z. Fan, *Adv. Energy Mater.*, 2014, **4**, 1300816.
13 W. Wei, X. Cui, W. Chen and D. G. Ivey, *Chem. Soc. Rev.*, 2011, **40**, 1697–1721.
14 K. K. Lee, W. S. Chin and C. H. Sow, *J. Mater. Chem. A*, 2014, **2**, 17212–17248.
15 G. S. Snook, P. Kao and A. S. Best, *J. Power Sources*, 2011, **196**, 1–12.
16 H. Cheng, A. D. Su, S. Li, S. T. Nguyen, L. Lu, C. Y. H. Lim and H. M. Duong, *Chem. Phys. Lett.*, 2014, **601**, 168–173.
17 D. P. Dubal, G. S. Gund, C. D. Lokhande and R. Holze, *ACS Appl. Mater. Interfaces*, 2013, **5**, 2446–2454.
18 D. Z. W. Tan, H. Cheng, S. T. Nguyen and H. M. Duong, *Mater. Technol.*, 2014, **29**, A107–A113.
19 J. Kim, K. H. Lee, L. J. Overzet and G. S. Lee, *Nano Lett.*, 2011, **11**, 2611–2617.
20 Y. Shan and L. Gao, *Mater. Chem. Phys.*, 2007, **103**, 206–210.
21 X. Wang, M. Li, Z. Chang, Y. Yang, Y. Wu and X. Liu, *ACS Appl. Mater. Interfaces*, 2015, **7**, 2280–2285.
22 X. Wang, X. Han, M. Lim, N. Singh, C. L. Gan, M. Jan and P. S. Lee, *J. Phys. Chem. C*, 2012, **116**, 12448–12454.
23 H. Xia, J. Feng, H. Wang, M. O. Lai and L. Lu, *J. Power Sources*, 2010, **195**, 4410–4413.
24 D. Zhao, Z. Yang, L. Zhang, X. Feng and Y. Zhang, *Electrochem. Solid-State Lett.*, 2011, **14**, A93.
25 Y. Fang, F. Jiang, H. Liu, X. Wu and Y. Lu, *RSC Adv.*, 2012, **2**, 6562–6569.
26 X. Li, W. Sun, L. Wang, Y. Qi, T. Guo, X. Zhao and X. Yan, *RSC Adv.*, 2014, **5**, 7976–7985.
27 G. Zhu, Z. He, J. Chen, J. Zhao, X. Feng, Y. Ma, Q. Fan, L. Wang and W. Huang, *Nanoscale*, 2014, **6**, 1079–1085.
28 Z. Tang, C. Tang and H. Gong, *Adv. Funct. Mater.*, 2012, **22**, 1272–1278.
29 J. Wu, P. Guo, R. Mi, X. Liu, H. Zhang, J. Mei, H. Liu, W. M. Lau and L. M. Liu, *J. Mater. Chem. A*, 2015, **3**, 15331–15338.
30 M. B. Bryning, D. E. Milkie, M. F. Islam, L. A. Hough, J. M. Kikkawa and A. G. Yodh, *Adv. Mater.*, 2007, **19**, 661–664.
31 H. Cheng and H. M. Duong, *RSC Adv.*, 2015, **5**, 30260–30267.
32 F. Wang, S. Xiao, Y. Hou, C. Hu, L. Liu and Y. Wu, *RSC Adv.*, 2013, **3**, 13059–13084.
33 C. Yang, M. Zhou and Q. Xu, *Phys. Chem. Chem. Phys.*, 2013, **15**, 19730–19740.
34 H. Xia, M. Lai and L. Lu, *JOM*, 2011, **63**, 54–59.
35 D. Li, F. Meng, X. Yan, L. Yang, H. Heng and Y. Zhu, *Nanoscale Res. Lett.*, 2013, **8**, 1–8.
36 G. Jian, Y. Xu, L. C. Lai, C. Wang and M. R. Zachariah, *J. Mater. Chem. A*, 2014, **2**, 4627–4632.
37 J. X. Feng, S. H. Ye, X. F. Lu, Y. X. Tong and G. R. Li, *ACS Appl. Mater. Interfaces*, 2015, **7**, 11444–11451.
38 L. Yang, S. Cheng, X. Ji, Y. Jiang, J. Zhou and M. Liu, *J. Mater. Chem. A*, 2015, 7338–7344.
39 Q. Wang, J. Yan and Z. Fan, *Energy Environ. Sci.*, 2016, **9**, 729–762.
40 D. P. Dubal, D. S. Dhawale, R. R. Salunkhe, S. M. Pawar and C. D. Lokhande, *Appl. Surf. Sci.*, 2010, **256**, 4411–4416.
41 J. Yang, X. Yang, Y. L. Zhong and J. Y. Ying, *Nano Energy*, 2015, **13**, 702–708.
42 F. Yang, M. Zhao, Q. Sun and Y. Qiao, *RSC Adv.*, 2015, **5**, 9843–9847.
43 J. Kim, K. H. Lee, L. J. Overzet and G. S. Lee, *Nano Lett.*, 2011, **11**, 2611–2617.
44 Z. Lei, J. Zhang and X. S. Zhao, *J. Mater. Chem.*, 2012, **22**, 153–160.

45 Y. Jin, H. Chen, M. Chen, N. Liu and Q. Li, *ACS Appl. Mater. Interfaces*, 2013, **5**, 3408–3416.
46 L. Li, Z. A. Hu, N. An, Y. Y. Yang, Z. M. Li and H. Y. Wu, *J. Phys. Chem. C*, 2014, **118**, 22865–22872.
47 Y. Cheng, S. Lu, H. Zhang, C. V. Varanasi and J. Liu, *Nano Lett.*, 2012, **12**, 4206–4211.
48 Y. Li and X. M. Li, *RSC Adv.*, 2013, **3**, 2398–2403.
49 W. Xing, S. Z. Qiao, R. G. Ding, F. Li, G. Q. Lu, Z. F. Yan and H. M. Cheng, *Carbon*, 2006, **44**, 216–224.